



ELSEVIER

Contents lists available at ScienceDirect

Journal of the Mechanics and Physics of Solids

journal homepage: www.elsevier.com/locate/jmps

Optimizing a fin ray for stiffness

Silas Alben^{a,*}, Reginald L. McGee^b^a School of Mathematics, Georgia Institute of Technology, Atlanta, GA, USA^b Department of Mathematics, Florida Agricultural and Mechanical University, Tallahassee, FL, USA

ARTICLE INFO

Article history:

Received 5 September 2009

Received in revised form

12 January 2010

Accepted 6 March 2010

Keywords:

Fin

Swimming

Biomechanics

Optimization

Strength

ABSTRACT

We optimize the elastic constants of the supporting structure in flexible fish fins—the fin ray—to obtain the least deflection under loading. We first solve the problem numerically for rays with shear layers of uniform thickness. The optimal distributions of bending and shear moduli are nonzero on disjoint regions. The numerical solution suggests the form of the analytical solution, which we obtain using calculus of variations on two intervals with continuity conditions at the interface. The deflection of the optimal ray is less than half that of the uniform ray. When the shear layer thickness is allowed to vary, we find a tapered thickness distribution which gives zero deflection for a given positive loading.

© 2010 Elsevier Ltd. All rights reserved.

1. Introduction

In this work we consider the optimization of the fin ray, the main structural component in the flexible fins of the most evolved fish. More than half of all fish species have fin rays (Alben et al., 2007). Flexible fins consist of a nearly parallel array of fin rays of varying lengths, shown in Fig. 1. Fin rays are present in most of the fins of a bluegill sunfish, shown in Figs. 1a and b. Figs. 1b and c show the rays in the pectoral fin, in a side view. The rays branch moving outward along the fin. Fig. 1d shows a schematic diagram of a single ray, composed of two bony rods which sandwich a thin layer of gel. The ray bends perpendicularly to the plane of the fin, and Fig. 1d shows views of the ray in its plane of bending. The rays are bound together in the fin by a stretchable skin membrane, labeled in Fig. 1e, which shows a cross-section through the fin. The expanded view in Fig. 1e shows the bilaminar structure of the rays, consisting of two segmented bony rods, called hemitrichs, which sandwich a layer of gel (width labeled d) which is densely interspersed with collagen fibers anchored in the bony segments. The cross sections of the bony segments in Fig. 1e are roughly semicircular. Muscles attach via tendons to each of the bases of the two rods where they meet the fish body. Actuation of the tendons by these muscles is shown by the arrows in Fig. 1d. The forces can rotate the entire fin ray at its base, and also bend the fin ray in a direction perpendicular to the plane of the fin. The distribution of curvature in a given ray is set by the distribution of bending stiffness in the two segmented rods, the distribution of shear stiffness in the collagenous layer between the rods, and the actuation by the muscles, which sets the relative position of the bases of the two rods. Videler (1993) and Alben et al. (2007) give additional background on the anatomy of fins and fin rays.

As a mechanical structure, the fin ray is interesting because it provides a simple strategy for transducing force into motion. Forces are applied only at one end of the ray, and tune the shape of the ray actively through a single parameter: the tangential shift between the rods at the base (the component of the difference in position of the bases of the two rods

* Corresponding author.

E-mail address: alben@math.gatech.edu (S. Alben).

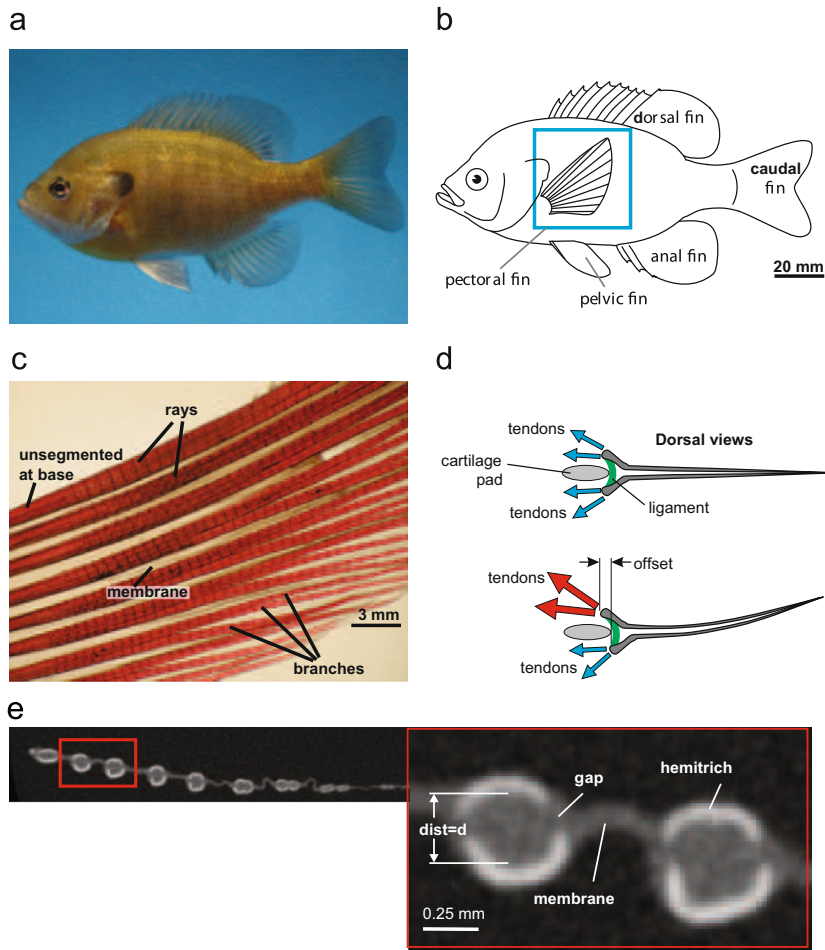


Fig. 1. (a) Photograph of a bluegill sunfish. (b) Schematic showing the location of the fish fins. The pectoral fin is highlighted with the blue box. (c) Photograph of a cleared and stained pectoral fin. The short bony segments can be seen along the length of the rays. (d) Schematic showing dorsal views of an individual fin ray with two body rods actuated by muscles and tendons. Muscles (not shown) exert forces on the tendons attached to the base of each body rod, and bend the ray perpendicular to the plane of the fin. (e) Single cross-section slice from a microCT scan of a pectoral fin. The left panel shows multiple rays and the right panel shows an expanded view of two rays. The bright white regions are bony areas and the gray is softer tissues (fin membrane and connective tissues). The separation between the two hemitrichs of the left ray is labeled “dist=d.” Reprinted from Alben et al. (2007). (For interpretation of the references to color in this figure legend, the reader is referred to the web version of this article.)

which is tangent to the rods). Artificial versions of the fin ray have recently been developed (Tangorra et al., 2007; Trease et al., 2003).

Under a transverse load, such as that due to fluid pressure forces, the ray resists deflection passively due to the combined bending modulus of the two rods and the shear modulus of the collagen layer. The resistance is increased dramatically when the bases of the rays are held fixed, and not allowed to shift freely. Cantilever tests reported in Alben et al. (2007) showed that the effective bending modulus can be increased by a factor of 10–100 when the bases of the ray are clamped. Clamping the bases increases the shear experienced by the collagenous layer, and also increases the effective area moment of inertia of the fin ray, similarly to sandwich structures (Vinson, 1999).

In this paper we solve a basic optimization problem for the fin ray. We use the mechanical model for the ray derived in Alben et al. (2007), which involves two elastic parameters and one geometrical parameter distributed along the ray. We optimize these parameters when the ray experiences static loading, with the bases held fixed as in the cantilever tests mentioned above. This provides a simple representation for how the fin ray can resist pressure forces in a steady (or quasi-steady) flow. The optimization problem provides some insight into how the fin ray should be designed to be as strong as possible under steady loading. The fin ray has evolved in a diverse range of unsteady flows during fish swimming, and future work will consider optimization problems which address unsteady motions. Fins perform an enormous variety of motions in swimming, such as flapping, rowing, steering, and cupping (Tangorra et al., 2007; Videler, 1993). Common to all of these motions is the resistance of fluid forces transverse to the fin ray, which is the problem we consider here, in a static situation. It is difficult to provide definitive explanations for biological structures using optimization problems, but these

problems can be useful for interpreting and quantifying many aspects of biological structures (Alexander, 1996; Squires, 2004; Yu et al., 2006; Alben, 2008; Noblin et al., 2008).

The fin ray can be viewed as a variation on the sandwich beam, which is used to achieve high strength-to-weight ratios in solid structures (Vinson, 1999). We approach the optimization of the fin ray with methods used in other structural optimization problems (Haftka and Gürdal, 1992; Keller, 1960).

The organization of the remaining sections is as follows. In Section 2, we summarize the mechanics of the fin ray, and specialize to small deflections. In Section 3, we pose the optimization problem for uniform spacing between the beams. We first solve the problem numerically, and then use the numerical solution to obtain the correct form for the analytical solution. In Section 4 we obtain the spacing between the beams which gives zero deflection for a given positive loading. Section 5 summarizes the results in the context of experimental observations.

2. Model

We consider the bending of the fin ray perpendicular to the plane of the fin, relevant to the resistance of loading by fluid pressure forces. Following Alben et al. (2007), the fin ray is modeled as a sandwich structure consisting of two elastic beams with positions $\mathbf{X}_1(s)$, $\mathbf{X}_2(s)$. Here s is arc length, $-1 \leq s \leq 1$ (so lengths are nondimensionalized by the beams' half-lengths), and we assume the beams bend but do not stretch. The beams have bending rigidity $B(s)$. The layer between the beams has thickness $d(s)$ (assumed $\ll 1$) and shear modulus $G(s)$. The shear modulus provides additional resistance to deflection of the sandwich structure.

In Fig. 2a, we show the schematic of the pectoral fin from Fig. 1b, with nine dashed lines showing the center lines of the nine fin rays. For two of the fin rays, we show also the symmetric pair of bony segmented beams in each ray as thick solid lines. The beams are displaced symmetrically from the center line, in the direction perpendicular to the plane of the fin. The arrows indicate the direction of bending, which is also perpendicular to the plane of the fin. In Figs. 2b–d, we show the fin ray in its plane of bending, in straight (b) and bent (c, d) states. The layer between the beams has uniform thickness d here, and is marked with vertical material lines to show how the layer between the beams is sheared in panels c and d. The fin rays in Fig. 2 are a model for the sandwich structures shown in Fig. 1d, which bend perpendicularly to the plane of the fin to resist fluid forces.

Fig. 2c shows the fin ray in a deformed state, where the two beams are held clamped at $s=0$ and flex upwards (as though loaded by an upwards force) to assume a shape with uniform curvature, equal to unity. In the flexed state the distance between the beams normal to the centerline remains d , due to the fluidized collagen fiber network in the layer between the beams which prevents them from coming apart as they flex (Alben et al., 2007). However, the layer between the beams undergoes significant shear, which is evident in the rotation of the solid material lines relative to the dashed material line. The upper beam is shifted forward relative to the lower beam at the end. The two beams are analogous to lanes on a curved running track. To cover equal distances in each lane, the finish line on the inner track (upper beam) is shifted forward relative to that on the outer track (lower beam). In Alben et al. (2007), an expression for this shift was derived:

$$\phi(s) \equiv (\mathbf{X}_2(s) - \mathbf{X}_1(s)) \cdot \hat{\mathbf{s}}_{\text{avg}}, \tag{2.1}$$

$$\phi(s) \approx \phi_{m1} - \int_{-1}^s d(s') \kappa_{\text{avg}}(s') ds'. \tag{2.2}$$

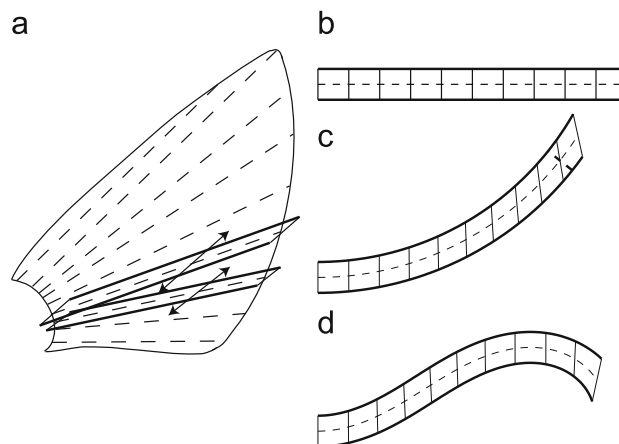


Fig. 2. (a) Schematic of a fin with nine fin rays. The center lines of the fin rays are the dashed lines. For two of the fin rays, we show the pair of bony segmented rods (hemitrichs) as thick solid lines, displaced symmetrically from the center lines in the direction perpendicular to the plane of the fin. The arrows indicate the main direction of bending of a fin ray, also perpendicular to the plane of the fin. (b) A top view of a fin ray from panel a, showing the fin ray in its plane of bending. (c, d) Bent states of a fin ray in its plane of bending. As in panels a and b, the top and bottom solid lines represent the beams with bending moduli $B(s)$ versus arc length s . The space between the beams represents a layer of collagenous gel with shear modulus $G(s)$.

Here $\phi(s)$ is defined as the shift of the lower beam with respect to the upper beam relative to the centerline between them (the dashed lines in Fig. 2), which has unit tangent \hat{s}_{avg} . In Eq. (2.2), ϕ_{m1} is the shift at $s = -1$, κ_{avg} is the curvature of the centerline, and the integral gives a good approximation (accurate to $O(d^3)$), while ϕ is $O(d)$. Eq. (2.2) shows that the shift between the beams grows with their curvature and the spacing between them, which is also observed on a running track.

In the examples shown in Fig. 2, d is uniform and ϕ_{m1} is zero, so Eq. (2.2) simplifies to

$$\phi(s) \approx -d\theta_{\text{avg}}(s). \quad (2.3)$$

Thus the shift is proportional to the tangent angle of the centerline. Fig. 2d is an example in which the tangent angle becomes zero at $s=0.75$, and there the shift ϕ and the shear (ϕ/d) are seen to be zero.

We shall now determine the distributions of material parameters B and G and geometric parameter d which minimize the deflection of the fin under a given static loading. We determine the shape of the fin ray by the extended Hamilton's principle, which requires setting to zero the variation of

$$J = \int_{-1}^1 \left[B(s')\kappa_{\text{avg}}(s')^2 + \frac{1}{2}G(s')\left(\frac{\phi(s')}{d(s')}\right)^2 - f(s')y(s') \right] ds', \quad (2.4)$$

with respect to y . J is the sum of internal elastic energies in bending and shear minus the work done by a vertical force per unit length $f(s)$. We now assume small deflections from the horizontal state, so the fin shape is described as $y(x)$. We have $\kappa_{\text{avg}}(s) \approx y'(x)$; $\theta_{\text{avg}}(s) \approx y'(x)$. We also assume the applied shift at the fin ray base, ϕ_{m1} , is zero, which corresponds to clamping the bases of the two ray halves together as in Alben et al. (2007). Then J simplifies to

$$J = \int_{-1}^1 \left[B(x_1)y''(x_1)^2 + \frac{1}{2}G(x_1)\left(\frac{1}{d(x_1)}\int_{-1}^{x_1} d(x_2)y''(x_2) dx_2\right)^2 - f(x_1)y(x_1) \right] dx_1. \quad (2.5)$$

Taking the variation of J with respect to y and integrating by parts, we obtain the ODE for y :

$$2(B(x)y''(x))'' - \left(d(x) \int_1^x \frac{G(x_1)}{d^2(x_1)} \left(\int_{-1}^{x_1} d(x_2)y''(x_2) dx_2 \right) dx_1 \right)'' = f(x), \quad (2.6)$$

as well as free-end boundary conditions at $x=1$:

$$M(1) = M'(1) = 0, \quad (2.7)$$

$$M(x) = 2By' + d(x) \int_1^x \frac{G(x_1)}{d^2(x_1)} \left(\int_{-1}^{x_1} d(x_2)y''(x_2) dx_2 \right) dx_1. \quad (2.8)$$

We assume the fin is clamped at $x = -1$, so $y(-1) = y'(-1) = 0$.

3. Uniform d

We first consider the case where the spacing d is uniform, and the loading f is also uniform and equal to unity (and hence B and G can be regarded as nondimensionalized by the appropriate combinations of the loading force magnitude and the fin length). Then (2.6) simplifies to

$$2(B(x)y''(x))'' - (G(x)y'(x))' = 1. \quad (3.1)$$

We seek B and G which minimize the integrated deflection

$$\int_{-1}^1 y(x) dx \quad (3.2)$$

under constraints of fixed integrated bending and shear moduli

$$\int_{-1}^1 B(x) dx = B_0; \quad \int_{-1}^1 G(x) dx = G_0. \quad (3.3)$$

We constrain B and G to be nonnegative by writing them as squares of real-valued functions:

$$B = b^2; \quad G = g^2. \quad (3.4)$$

The Lagrangian to be minimized is

$$L = \int_{-1}^1 y dx - \int_{-1}^1 \lambda_1(x)(2(b^2 y'')'' - (g^2 y')' - 1) dx, \quad (3.5)$$

$$- \lambda_2 \left(B_0 - \int_{-1}^1 b^2 dx \right) - \lambda_3 \left(G_0 - \int_{-1}^1 g^2 dx \right). \quad (3.6)$$

Taking the variations with respect to y , b , and g yields

$$2(b^2\lambda_1'')'' - (g^2\lambda_1')' = 1, \quad (3.7)$$

$$2b\lambda_1''y'' = b\lambda_2, \quad (3.8)$$

$$g\lambda_1'y' = -g\lambda_3, \quad (3.9)$$

respectively. Taking the variations with respect to the Lagrange multipliers λ_1 , λ_2 , and λ_3 gives the corresponding constraints.

If we assume that B and G do not vanish on the fin ray, we may cancel b and g from (3.8) and (3.9), and combine the equations to obtain

$$y'' = \sqrt{\frac{\lambda_2}{2\lambda_3}}y', \quad (3.10)$$

and the same equation for λ_1 . The only solution satisfying the clamped boundary conditions is the zero solution, which is incompatible with the original Eq. (3.1). To obtain additional information we now solve the problem numerically.

3.1. Numerical optimization

To enforce the constraints (3.3) it is natural to approximate b and g by their truncated Fourier–Legendre series:

$$b(x) = \sum_{j=0}^m b_j P_j(x); \quad g(x) = \sum_{j=0}^m g_j P_j(x). \quad (3.11)$$

By orthogonality of the P_j (assumed to be normalized), the constraints (3.3) simplify to

$$\sum_{j=0}^m b_j^2 = B_0; \quad \sum_{j=0}^m g_j^2 = G_0. \quad (3.12)$$

We express the coefficients $\{b_j\}$ and $\{g_j\}$ as points on m -spheres of radii $\sqrt{B_0}$ and $\sqrt{G_0}$. Our constrained optimization problem is then transformed to an unconstrained problem when we use the angular coordinates on the spheres as the variables. We thus minimize the integrated deflection (3.2) over solutions to the discretized version of the ODE (3.1). We discretize the interval $[-1,1]$ as a uniform grid and use the trapezoidal rule to compute (3.2). Given the spherical coordinates, we compute B and G , and solve for y on the grid by solving the discretized version of the ODE (3.1) as a matrix equation for y . The discretization is accurate to second-order in the grid spacing and preserves the positive semidefiniteness of the elastic terms in the energy (2.5). The latter property is important to prevent convergence to spurious numerical solutions which have negative mean deflections and which do not persist as the grid is refined.

As initial guesses, we choose points at random on the spheres and move them according to the Broyden–Fletcher–Goldfarb–Shanno (BFGS) method for minimization, which is Hessian-free (Broyden, 1970). We run the method until stagnation, starting from many initial guesses, and select the solution which minimizes the integral of y . We perform this routine for m ranging from 2 (in which case b and g are quadratic polynomials) to 40. The optimal solutions for B , G and y are shown in Fig. 3a for $m=2, 3, 4, 5, 10, 15$, and 20, $B_0=1/2$, $G_0=1$. Thicker lines correspond to larger m . As m increases, the shapes seem to converge to a particular solution. The most notable feature is that B and G seem to segregate: B is essentially zero for $x \gtrsim 0$ and G is essentially zero for $x \lesssim 0$. B is largest near the clamped end, and decreases moving outward. Near $x=0$, G increases sharply from zero to a finite value, and then decreases towards zero with an oscillatory behavior.

Fig. 3b gives the integral of y for the solutions in panel a. Since the spaces of Fourier–Legendre series for increasing m are nested, the best (mathematical) solution at a given m is at least as good as the best solution at all smaller m . Thus we would expect the integral of y to decrease with increasing m . For the computed solutions, the integral decreases monotonically as m increases up to 20, and then stagnates. Although the mathematical solution is better at larger m , computing it in a given amount of time is more difficult because the search is conducted in a space of higher dimension, and each step of the minimization routine takes longer.

After Eq. (3.10), we noted that if b and g are nonzero, there is apparently no solution to the optimization problem. The numerical solution indicates that b and g are in fact zero on subintervals which nearly partition the interval $-1 \leq x \leq 1$. This motivates us to search for an analytical solution where the supports of b and g exactly partition the interval.

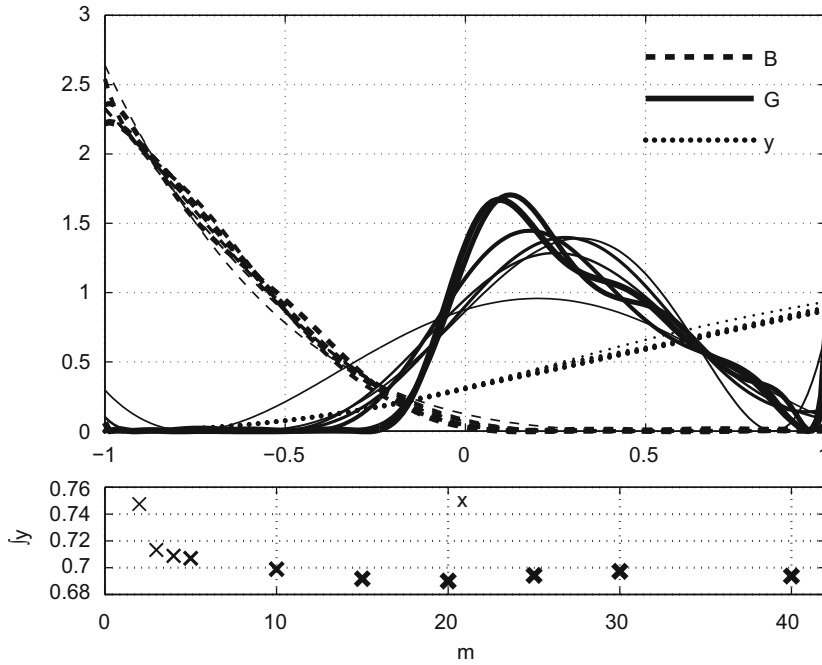


Fig. 3. (a) Computed optimal B (dashed lines), G (solid lines), and y (dotted lines) for $m=2, 3, 4, 5, 10, 15, 20, B_0=1/2, G_0=1$. Values for larger m are plotted with thicker lines. (b) Integral of y for the shapes in (a) and those found with larger m .

3.2. Analytical optimization

We seek a solution for which b is nonzero only on the interval $-1 \leq x < a$, and g is nonzero only on $a < x < 1$, for some $a : -1 \leq a \leq 1$. In this case, (3.1), (3.7)–(3.9) become

$$\left. \begin{aligned} 2(By''')' &= 1 \\ 2(B\lambda_1''')' &= 1 \\ 2\lambda_1''y'' &= \lambda_2 \end{aligned} \right\} -1 < x < a, \quad (3.13)$$

$$\left. \begin{aligned} -(Gy')' &= 1 \\ -(G\lambda_1')' &= 1 \\ \lambda_1'y' &= -\lambda_3 \end{aligned} \right\} a < x < 1. \quad (3.14)$$

The solution to Eqs. (3.13) is given by [Haftka and Gurdal \(1992\)](#) with different boundary conditions. The solution to equations (3.14) is obtained similarly, and because of the boundary conditions it is most convenient to solve (3.14) first.

The free end boundary condition (2.7) at $x=1$ implies that

$$2(By''')' - (Gy')|_1 = -(Gy')|_1 = 0 \quad (3.15)$$

and the same with λ_1 in place of y . Integrating the first two Eqs. (3.14) with this boundary condition, and combining with the third Eq. (3.14),

$$Gy' = G\lambda_1' = 1 - x, \quad (3.16)$$

$$G = \frac{2G_0}{(1-a)^2}(1-x), \quad a < x < 1, \quad (3.17)$$

$$G = 0, \quad -1 < x < a. \quad (3.18)$$

The prefactor in G (Eq. (3.17)) is determined by the constraint (3.3).

Turning now to Eqs. (3.13), we integrate the first two of (3.13):

$$2(By''')' = 2(B\lambda_1''')' = x + c. \quad (3.19)$$

The constant c is determined by the requirement that $2(By'')' - Gy'$ be continuous at $x=a$, since its derivative equals 1 there, by Eq. (3.1). Using (3.16), we have

$$2(By'')' = 2(B\lambda_1'')' = x-1. \tag{3.20}$$

Partitioning the energy integral into integrals over the subintervals and taking the variations with respect to y yields a second boundary condition at $x=a$:

$$2By''|_a = 0 \tag{3.21}$$

and similarly for λ_1 . This provides the constant of integration when we integrate (3.20):

$$2By'' = 2B\lambda_1' = \frac{1}{2}[(x-1)^2 - (a-1)^2]. \tag{3.22}$$

Inserting into the third of Eqs. (3.13) gives

$$B = \frac{3B_0[(x-1)^2 - (a-1)^2]}{4 + 6a - 2a^3}, \quad -1 < x < a, \tag{3.23}$$

$$B = 0, \quad a < x < 1.$$

B is normalized according to (3.3). We may now solve for the deflection y corresponding to the optimal B (3.23) and G (3.17) by integrating Eqs. (3.16) and (3.22). The constants of integration are fixed by the conditions that y is clamped at $x = -1$ and continuous at $x = a$:

$$y = \frac{2 + 3a - a^3}{12B_0}(x+1)^2, \quad -1 < x < a, \tag{3.24}$$

$$y = \frac{(1-a)^2}{2G_0}(x-a) + \frac{(a+1)^2(2+3a-a^3)}{12B_0}, \quad a < x < 1. \tag{3.25}$$

The integrated deflection is

$$\int_{-1}^1 y(x) dx = \frac{(1+a)^4(-2+a)^2}{18B_0} + \frac{(-1+a)^4}{4G_0} \equiv \frac{1}{G_0} F\left(a; \frac{G_0}{B_0}\right). \tag{3.26}$$

We define the integrated deflection (3.26) as a function F of a and the parameter G_0/B_0 , the ratio of integrated shear to integrated bending modulus. The minimizer of F is a root of

$$\frac{dF}{da} = \left[\frac{(1+a)^3(-2+a)}{3B_0} + \frac{(-1+a)^2}{G_0} \right] (-1+a). \tag{3.27}$$

For any G_0/B_0 , dF/da vanishes at $a=1$ and at one point a^* interior to $[-1,1]$, which is the global minimizer of F . Because dF/da is a quintic polynomial in a and the root $a=1$ is known, a^* can be written in closed form in terms of G_0/B_0 as the root of a quartic. We omit the quartic root formula, which is lengthy, but plot a^* versus G_0/B_0 in Fig. 4. As G_0/B_0 increases, a^* decreases, which is intuitive: the region of positive shear modulus becomes larger than the region of positive bending

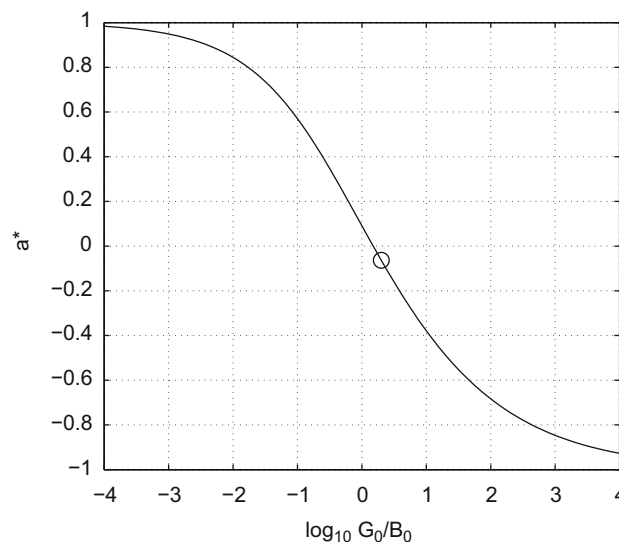


Fig. 4. Value of a which minimizes the integrated deflection of the fin.

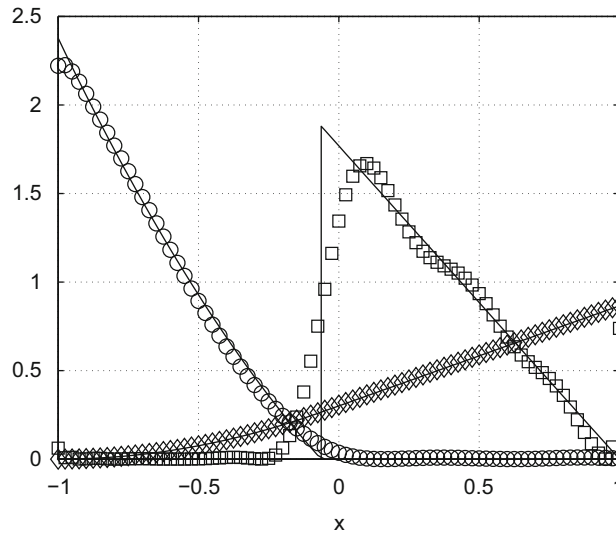


Fig. 5. Comparison between the analytical solution (solid lines) and the computed optimal fin solution with $m=20$, in terms of B (circles), G (squares), and y (diamonds).

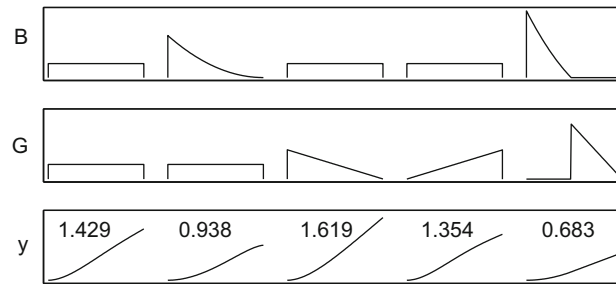


Fig. 6. Comparison between four simple solutions (columns 1–4) and the optimum solution (fifth column), for $B_0=1/2$ and $G_0=1$. B is uniform in the first, third, and fourth columns, and is $3(1-x)^2/16$ in the second column. G is uniform in the first and second columns, is $2(1-x)$ in the third column, and is $2(1+x)$ in the fourth column.

modulus because there is relatively more shear modulus available. The asymptotic behavior of a^* at small and large G_0/B_0 can be read off from the first factor on the right side of (3.27):

$$1-a^* = O\left(\left(\frac{G_0}{B_0}\right)^{1/2}\right), \quad \frac{G_0}{B_0} \ll 1; \quad 1+a^* = O\left(\left(\frac{G_0}{B_0}\right)^{-1/3}\right), \quad \frac{G_0}{B_0} \gg 1. \quad (3.28)$$

For the example plotted in Fig. 3, $G_0/B_0=2$. Here $a^* = -0.06328$ and the integrated deflection is 0.6837, shown by the circle in Fig. 4. This value is slightly below the integrated deflections for the computed solutions in Fig. 3b. The least integrated deflection for a computed solution is 0.6901, which was found with $m=20$. We plot this computed solution in Fig. 5 (open symbols) together with the analytical solution (solid lines), and find good agreement. The error is largest for the jump in G at a^* , due to the smoothness of the approximating polynomial.

To see the difference between the optimal solution and some simple distributions of B and G , in Fig. 6 we compare the optimal solution with four simple distributions of B and G consisting of constant, linear, and quadratic functions. The quadratic function B in the second column is the optimum when G is uniformly zero. The linearly tapered G in the third column is the optimum when B is uniformly zero. When B is nonzero, as here, an inversely tapered G is better (fourth column). The values plotted above the y curves are the integrated deflections, which show that the differences between the optimum and these other simple stiffness distributions can be substantial.

4. Nonuniform d

We now return to the case where the spacing between the beams, d , is nonuniform. The fin deflection is given by Eq. (2.6). The deflection's dependence on d is somewhat more complex than its dependences on B and G , because of the

integral in which d appears in Eq. (2.5). For a given loading f in (2.6), we now show that it is possible to choose d so that the deflection y is zero. We first integrate both sides of (2.6) twice from the free end:

$$2B(x)y''(x) - d(x) \int_1^x \frac{G(x_1)}{d^2(x_1)} \left(\int_{-1}^{x_1} d(x_2)y'(x_2) dx_2 \right) dx_1 = \int_1^x \int_1^{x_1} f(x_2) dx_2 dx_1, \quad (4.1)$$

where the constants of integration vanish due to the free-end boundary conditions (2.7). We then divide by d and differentiate the equation:

$$\left(\frac{2B(x)}{d(x)} y''(x) \right)' - \frac{G(x)}{d^2(x)} \int_{-1}^x d(x_1)y'(x_1) dx_1 = \left(\frac{\int_1^x \int_1^{x_1} f(x_2) dx_2 dx_1}{d(x)} \right)'. \quad (4.2)$$

If we now set $d(x)$ equal to the numerator of the fraction on the right side of (4.2), the right side is the derivative of a constant, or zero. Since the left side is homogeneous in y , a solution for y is the zero function. As long as the double integral of f on the right side of (4.2) is uniformly positive, so is the spacing d , which yields a geometrically realistic spacing function. Such is the case when f is a positive function, for example. For uniform loading $f \equiv 1$, the spacing giving zero deflection is $d = (x-1)^2/2$, which tapers quadratically at the free end. For any uniformly positive f , d decreases monotonically to zero at the end, and decreases faster than linearly, because its curvature f is positive. In reality the fin ray is subjected to a wide range of loads. However, we hypothesize that certain d will lead to relatively small deflections for certain classes of biologically important loads.

5. Conclusion

We have posed and solved a simple optimization problem for the fin ray under steady loading. The ray is a cantilevered sandwich structure. We have fixed the total amounts of shear and bending modulus in the structure, and optimized their distributions first numerically and then analytically, using crucial insights from the numerical solutions. When the spacing between the beams is uniform, the regions where the two moduli are different from zero are disjoint, i.e. they do not overlap. The bending modulus occupies the subinterval adjacent to the clamped end, and is a quadratic polynomial which tapers to zero at the distal end of its support. The shear modulus occupies the complementary subinterval adjacent to the free end, and tapers linearly to zero at the free end.

At the interface between the two subintervals, the deflection and its slope are continuous, as well as the combinations of higher derivatives that appear in the free end boundary conditions. These continuity conditions were also used to fix unknown constants in the shear and bending modulus distributions. The position of the interface between the subintervals was found in terms of the elastic parameters, and is a root of a quartic polynomial. As the ratio of total elastic moduli tends to zero and ∞ , the interface position approaches the endpoints as a square root and as an inverse cubic root of the ratio, respectively.

We have also included the distribution of spacing between the beams in the optimization. We have found that zero deflection is obtained when the spacing is the double integral of the loading function, integrated from the free end.

Some aspects of these optimal solutions are very similar to what has been observed in real fin rays. In Alben et al. (2007), we found that the bending modulus tapers to very small values well before the free end of the fin ray. The shear modulus has not yet been measured experimentally, but it may account for the resistance that a fin ray can provide near its free end. Photographs of fin rays from pectoral and caudal fins show that the spacing between the rods also tapers significantly moving towards the free end (Alben et al., 2007; Videler, 1993). Future work will consider optimization problems with unsteady loading, such as that from a moving fluid.

References

- Alben, S., 2008. Optimal flexibility of a flapping appendage at high Reynolds number. *Journal of Fluid Mechanics* 614, 355–380.
- Alben, S., Madden, P.G., Lauder, G.V., 2007. The mechanics of active fin-shape control in ray-finned fishes. *Journal of the Royal Society Interface* 4 (13), 243–256.
- Alexander, R.M.N., 1996. *Optima for Animals*. Princeton University Press, Princeton, NJ, USA.
- Broyden, C.G., 1970. The convergence of a class of double-rank minimization algorithms 1. general considerations. *IMA Journal of Applied Mathematics* 6 (1), 76–90.
- Haftka, R.T., Gürdal, Z., 1992. *Elements of Structural Optimization*. Kluwer, Boston.
- Keller, J.B., 1960. The shape of the strongest column. *Archive for Rational Mechanics and Analysis* 5 (1), 275–285.
- Noblin, X., Mahadevan, L., Coomaraswamy, I.A., Weitz, D.A., Holbrook, N.M., Zwieniecki, M.A., 2008. Optimal vein density in artificial and real leaves. *Proceedings of the National Academy of Sciences* 105(27), 9140.
- Squires, T.M., 2004. Optimizing the vertebrate vestibular semicircular canal: could we balance any better? *Physical Review Letters* 93 (19), 198106.
- Tangorra, J.L., Davidson, S.N., Hunter, I.W., Madden, P.G.A., Lauder, G.V., Dong, H., Bozkurtas, M., Mittal, R., 2007. The development of a biologically inspired propulsor for unmanned underwater vehicles. *IEEE Journal of Oceanic Engineering* 32 (3), 533–550.
- Trease, B.P., Lu, K.J., Kota, S., 2003. Biomimetic compliant system for smart actuator-driven aquatic propulsion: preliminary results. 2008 ASME International Mechanical Engineering Congress & Exposition 68, 43–52.
- Videler, J.J., 1993. *Fish Swimming*. Springer, New York.
- Vinson, J.R., 1999. *The Behavior of Sandwich Structures of Isotropic and Composite Materials*. CRC Press, New York.
- Yu, T.S., Lauga, E., Hosoi, A.E., 2006. Experimental investigations of elastic tail propulsion at low Reynolds number. *Physics of Fluids* 18, 091701.